



A flapping vortex generator for heat transfer enhancement in a rectangular airside fin



Zheng Li^a, Xianchen Xu^a, Kuojiang Li^a, Yangyang Chen^a, Guoliang Huang^{a,*}, Chung-lung Chen^{a,*}, Chien-Hua Chen^b

^aMechanical and Aerospace Engineering, University of Missouri-Columbia, Columbia, MO, 65201, USA

^bAdvanced Cooling Technologies, Inc., Lancaster, PA 17601, USA

ARTICLE INFO

Article history:

Received 18 July 2017

Received in revised form 9 November 2017

Accepted 13 November 2017

ABSTRACT

This paper presents a two-dimensional numerical study of a novel flapping vortex generator mounted on a heatsink fin for airside heat transfer enhancement. The proposed vortex generator is made with a thin elastic sheet bonded to the inner wall of the heatsink channel with an inclined angle. Our investigations are focused on the effects of the Young's Modulus of the vortex generator on the oscillations of the elastic sheet, vorticity fields, and heat transfer performances. The results are compared with the heat transfer performances of conventional rigid agitators at two different flow velocities (Reynolds numbers). Our numerical results demonstrate that the vortex generator with a Young's Modulus of 1 MPa has the best performance among the other three choices and can enhance the rejected heat by 140% at the same velocity and 87% at the same total pumping power. The developed flapping vortex generator can improve the average Nusselt number by 200% compared with a clean channel with the same Reynolds number. Modal analysis is performed with transient temperature and vorticity results using dynamic modal decomposition where it is found that a steady modal behavior directly influences the thermal performance of the system. Furthermore, creating more discrete patterns near the boundaries of the steady mode in the vorticity field can enhance the internal convective heat transfer rate. The numerical results presented can help to guide the design of the flapping vortex generators in future high-performance airside fins.

© 2017 Elsevier Ltd. All rights reserved.

1. Introduction

Thermoelectric power generation plays an important role in the U.S., and during 20th century, its huge water consumption was acceptable. However, in recent years, several regions within the U.S. have experienced limited fresh water because of the fast growing population, industry, farming, aquaculture and drought. Saving fresh water has become more important than at any previous time. Much research has been devoted to capturing the fresh water [1]. Current thermoelectric water consumption is approximately 139 billion gallons per day (BGD), or 41% of all fresh water withdrawal, making it the largest single use of fresh water in the U.S. [2]. Of the fresh water withdrawn for the thermoelectric sector, 4.3 BGD is dissipated to the atmosphere by cooling towers and spray ponds (wet cooling). Approximately 1% of thermoelectric power plants in the U.S. use air-cooled condensers (dry cooling). Increasing the dry cooling ratio could save a significant amount of fresh water.

The airside convective heat transfer coefficient (10–100 W/m²K) is roughly two orders of magnitude lower than that for water (1000–10,000 W/m²K), depending on the operating regime. To reject the same amount of heat as wet cooling, dry cooling requires a much higher heat exchanger surface and pumping power. It is of critical importance to improve the airside heat transfer coefficient to make dry cooling more widespread. To achieve this, it is critical to improve the airside heat transfer coefficient.

Airside convective heat transfer includes natural convection and forced convection, distinguished by the driven power [3–6]. Considering the application of dry cooling in power plants, only forced convection is considered in this article. Many strategies exist to enhance airside heat transfer, such as offset strip fins, T-mixers, Dean flow in curved pipes and vortex generators. In general, modifying the flow channel and adding vortex generators are the two main categories. It is necessary to replace the current heat exchanger to improve the thermal performance by modifying the flow channel. The cost of replacing the current heat exchangers is too high, however, retrofitting vortex generators is feasible. The aim of this work is to improve the air side heat transfer in thermoelectric power plants.

* Corresponding authors.

E-mail addresses: HuangG@Missouri.edu (G. Huang), ChenCL@Missouri.edu (C.-l. Chen).

Nomenclature

A_m	amplitude of the free end in y direction (m)	p	pressure (Pa)
c_D	average drag coefficient (-)	St	Strouhal number (-)
c_p	specific heat (J/K)	T	temperature (K)
D	diameter of the rigid cylinder (m)	u	velocity in x direction (m/s)
D_h	Hydraulic diameter (m)	\vec{u}_s	motion of vortex generator (m)
E	Young's modulus (Pa)	v	velocity in y direction (m/s)
E^*	nondimensional Young's modulus (-)	V	velocity magnitude (m/s)
h	local heat transfer coefficient (W/mK)	λ	Lame's first parameter (Pa)
h_{ave}	local heat transfer coefficient (W/mK)	μ_s	Lame's second parameter (Pa)
H	2-D channel height (m)	μ	viscosity (Pa s)
k	thermal conductivity (W/m ² K)	ρ_0	air density (kg/m ³)
L	2-D channel length (m)	ρ_f	fluid density (kg/m ³)
Nu_{ave}	average Nusselt number (-)	ρ_s	solid density (kg/m ³)

Many types of vortex generators for heat transfer enhancement have been investigated. In general, stationary vortex generators and flapping vortex generators are the two main categories. For various stationary designs, transverse or longitudinal vortices can be generated for heat transfer enhancement [7–18]. Numerical and experimental results have demonstrated stationary agitators can enhance the convective heat transfer. Most stationary vortex generators are fabricated by modifying the channel surface and multiple stationary agitators are needed to reach desired thermal performance. Therefore there are not retrofitted.

Instead of modifying the channel surface, flapping vortex generator made of elastic material can be placed in the existing channel directly. Flapping vortex generators oscillate in the channel to create vortices for heat transfer enhancement. Two ways exist to fulfill the flapping vortex generators; the active method with external power and the passive method with fluid-structure interaction. Active flapping vortex generators have been employed to enhance heat transfer in different applications [19–22]. These active vortex generators can be applied to the current heat exchangers where their oscillating frequencies directly affect the thermal performance. However, active vortex generators require an additional power supply system to drive structure oscillation, limiting their application range. In recent years, fluid-structure interaction FSI) has been a topic of interest in many engineering fields [23–29].

Researchers have made great efforts to use passive flapping vortex generators for heat transfer enhancement [30–34]. In these investigations, the elastic structures are placed between the heat exchanger fins for heat transfer enhancement. Vibrating microfin array located on the fin has been discussed for heat transfer enhancement in laminar region and 10% heat transfer rate enhancement is reached at the same velocity [35]. The elastic structure mounted on the heat exchanger fins can enhance the heat transfer significantly and mounting multiple elastic structures on the fin have been discussed by others [36–37]. Stiffness has a significant impact on the FSI process [38]. However, thermal performance related to the material properties has not been

studied for this type of flapping vortex generator. To fill this gap, three flapping vortex generators with different Stiffness are compared for heat transfer enhancement.

Internal convective heat transfer can be enhanced by the vortices, which can reduce the thermal boundary layer. However, the quantitative relation between vortices and temperature field is still lacking, which can be the fundamental key to internal convective heat transfer. In recent years, modal analysis has been introduced to understand the coherent structures in the fluid flow, as discussed in a comprehensive review paper [39]. In this article, modal analysis is conducted to explore the fundamental of internal convective heat transfer related with vorticity field.

2. Physical model

Straight plate fins are widely used as an air-side heat exchanger. When the ratio between the fin height and fin gap is over 10, the 2-D assumption is valid, which is the condition in this article. The physical model is shown in Fig. 1 where the top and bottom boundaries represent the fins in the heat exchanger. The channel height, H, and length, L, with nonslip top and bottom boundaries with a constant temperature T_{wall} . The inlet has a constant

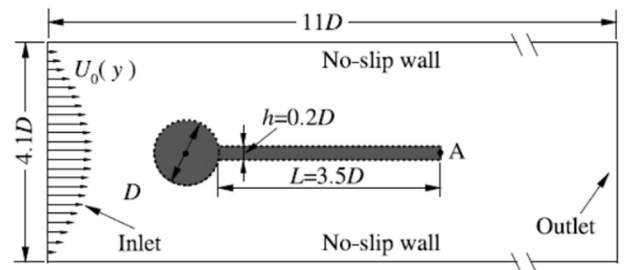


Fig. 2. Flow-induced vibration of an elastic beam behind a cylinder.

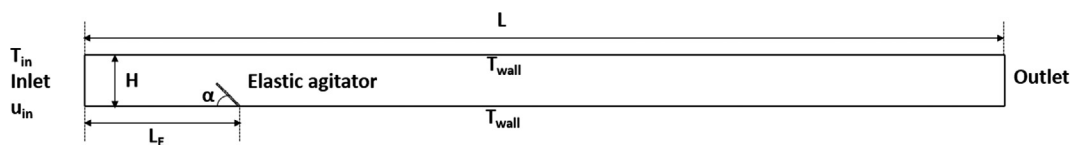


Fig. 1. Physical model.

temperature, T_{in} , constant velocity, u_{in} , and the outlet assumes ambient pressure. One elastic agitator is mounted on the bottom of the channel at an inclined angle α , and can vibrate due to the fluid structure interaction process acting as a flapping vortex generator. Correspondingly, vortices are generated and transferred in the channel for heat transfer enhancement. If laminar air flow is considered [40–41], the governing equations for the fluid flow and heat transfer are

$$\frac{\partial u}{\partial x} + \frac{\partial v}{\partial y} = 0 \tag{1}$$

$$\rho_0 \left(\frac{\partial u}{\partial t} + u \frac{\partial u}{\partial x} + v \frac{\partial u}{\partial y} \right) = -\frac{\partial p}{\partial x} + \mu \left(\frac{\partial^2 u}{\partial x^2} + \frac{\partial^2 u}{\partial y^2} \right) \tag{2}$$

$$\rho_0 \left(\frac{\partial v}{\partial t} + u \frac{\partial v}{\partial x} + v \frac{\partial v}{\partial y} \right) = -\frac{\partial p}{\partial y} + \mu \left(\frac{\partial^2 v}{\partial x^2} + \frac{\partial^2 v}{\partial y^2} \right) \tag{3}$$

$$\rho_0 c_p \left(\frac{\partial T}{\partial t} + u \frac{\partial T}{\partial x} + v \frac{\partial T}{\partial y} \right) = k \left(\frac{\partial^2 T}{\partial x^2} + \frac{\partial^2 T}{\partial y^2} \right) \tag{4}$$

$$\begin{cases} x = 0, & u = u_{in}, & v = 0, & T = T_{in} \\ x = L, & p = p_{ambient}, & \partial T / \partial x = 0 \\ y = 0, & u = 0, & v = 0, & T = T_{wall} \\ y = H, & u = 0, & v = 0, & T = T_{wall} \end{cases} \tag{5}$$

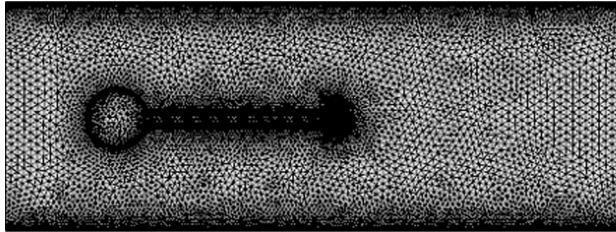
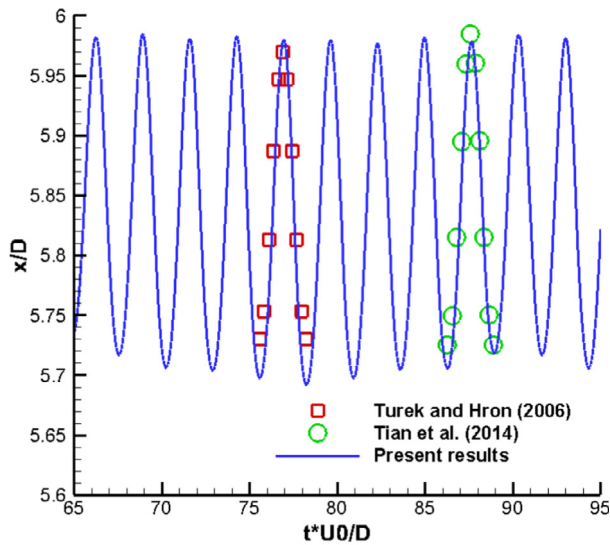
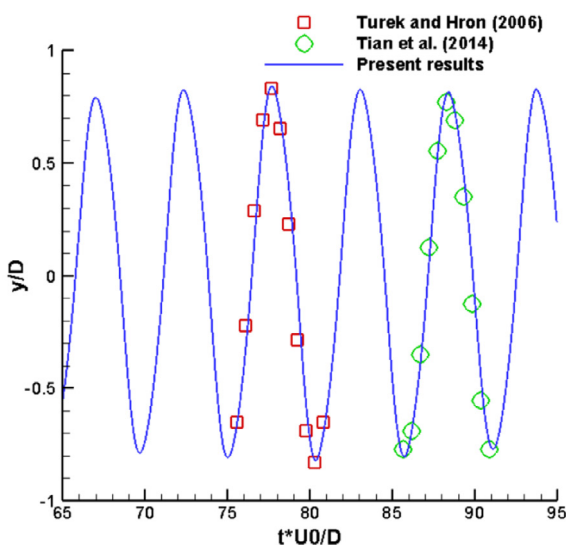


Fig. 3. Selected grid after independence study.



(a) Horizontal displacement

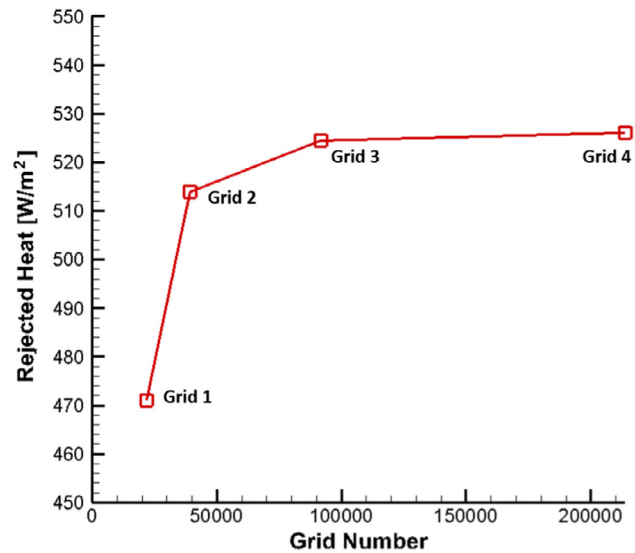


(b) Vertical displacement

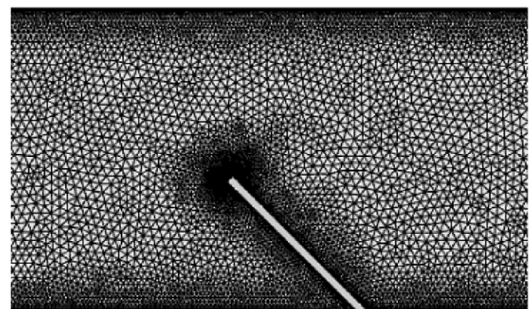
Fig. 4. Structure displacements compared with reference results.

Table 1
Results comparison in flow-induced vibration of the beam attached to a cylinder.

	A_m/D	St	C_D
Turek and Hron [43]	0.83	0.190	4.13
Tian et al. [42]	0.78	0.190	4.11
Present results	0.81	0.183	4.05



(a) Rejected heat comparison with different grids



(b) Selected grid near the vortex generator

Fig. 5. The comparison of different grids results.

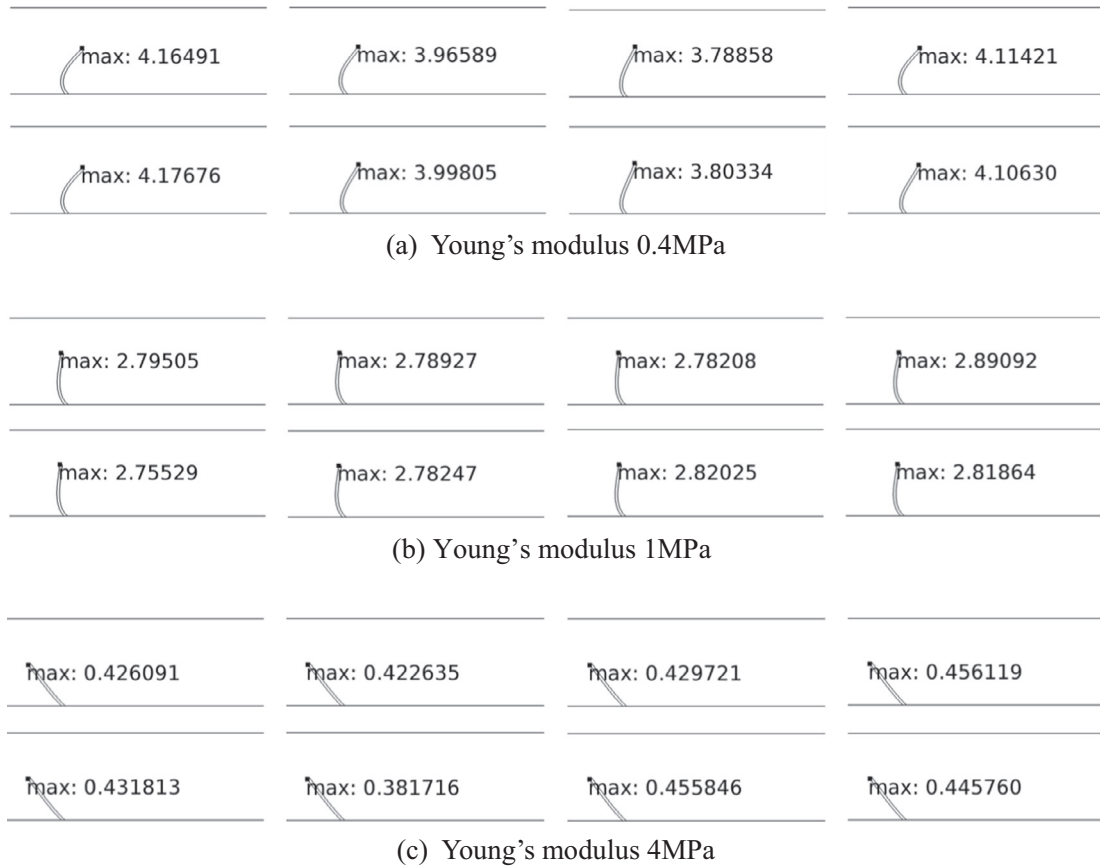


Fig. 6. Elastic agitator motion in test case1.

where u and v are velocities in x and y -direction, respectively. T and p are the fluid temperature and pressure. k , ρ_0 , c_p and μ are thermal conductivity, density, specific heat and viscosity determined by the fluid properties, respectively.

To describe the oscillation of the two-dimensional elastic flapping vortex generator under the air flow, the equations of motion can be written as,

$$(\lambda + \mu_s)\nabla\nabla \cdot \vec{u}_s + \mu_s\nabla^2\vec{u}_s = \rho_s\ddot{\vec{u}}_s \quad (6)$$

where displacement $\vec{u}_s = [u_1, u_2]^T$. The continuous boundary conditions of the velocity and stress fields on the surfaces of the elastic sheet must satisfy

$$\begin{cases} \vec{v} = \vec{u}_s \\ \vec{\sigma} \cdot \vec{n} = \vec{\Gamma} \cdot \vec{n} \end{cases} \quad (7)$$

where the stress in the solid is $\vec{\sigma} = \mu_s[(\nabla\vec{u}_s)^T + \nabla\vec{u}_s] + \frac{1}{2}\text{tr}[(\nabla\vec{u}_s)^T + \nabla\vec{u}_s]\vec{I}$ and the stress in the fluid is $\vec{\Gamma} = -p\vec{I} + \mu[(\nabla\vec{v})^T + \nabla\vec{v}] - \frac{2}{3}\mu(\nabla \cdot \vec{v})\vec{I}$ with $\vec{v} = [u, v]^T$. Eq. (7) can be used to describe the fluid-structural interactions in the numerical simulations.

3. Validation of numerical method

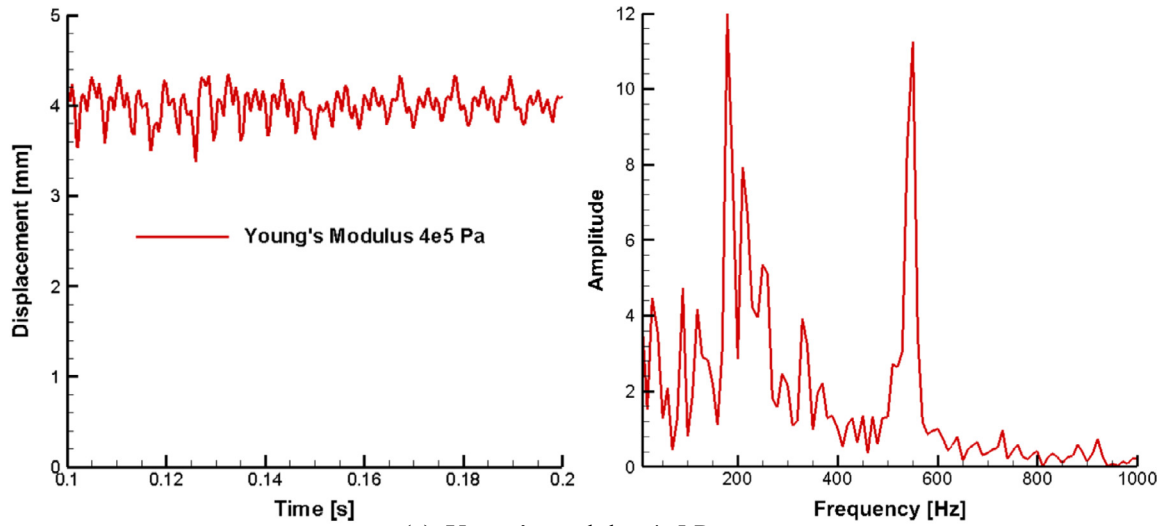
The commercial software COMSOL Multiphysics is employed to simulate the FSI process. To verify the numerical method, flow-induced vibration of an elastic beam behind a cylinder (shown in Fig. 2) is calculated and the results are compared with available Refs. [42–43]. An elastic beam is attached to a stationary rigid

cylinder, and the geometric parameters are shown in Fig. 2. The top and bottom boundaries are defined with a non-slip condition, while the inlet has a parabolic velocity profile. The average inlet velocity is \bar{U}_0 , which is used to calculate the Reynolds number (Re). In the validation, $Re = 100$ while the ratio between structure and fluid densities is $\rho_s/\rho_f = 10$. The non-dimensionalized Young's Modulus is defined as $E^* = E/\rho_f\bar{U}_0^2 = 1400$. After conducting a grid independent study, the grids shown in Fig. 3 is selected.

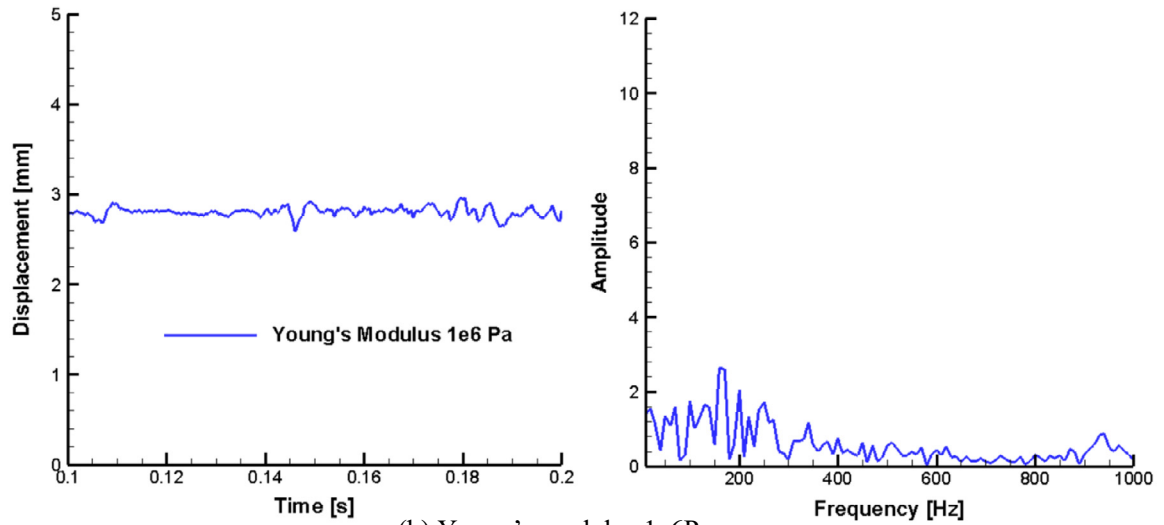
Fig. 4 shows the horizontal and vertical displacements for the chosen point A (marked in Fig. 2) which agree very well with the previous work by [42–43]. The amplitude of the free end in y -direction denoted by A_m , the Strouhal number defined as $St = fD/\bar{U}_0$ (f is the oscillation frequency), and the average drag coefficient $C_D = \bar{F}_x/(0.5\rho_f\bar{U}_0^2D)$ are compared with reference results as shown in Table 1. Very good agreements are obtained for all these three parameters and therefore, the numerical method is valid to solve FSI with large deformations.

4. Results and discussion

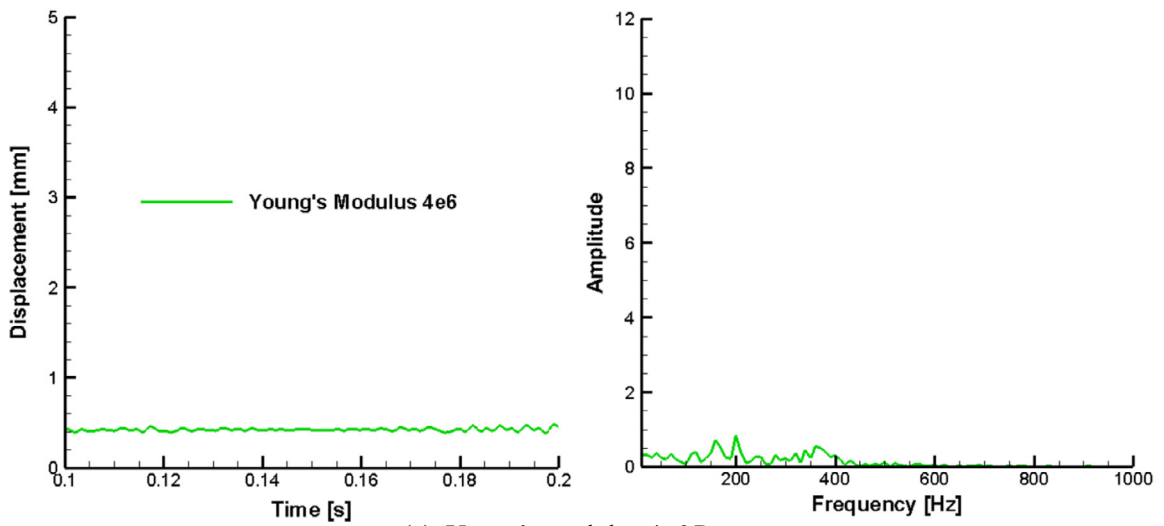
The verified numerical method is employed to solve the FSI coupled with heat transfer problem shown in Fig. 1. In the simplified 2-D model, the channel height, H , and channel length, L , are 6.6 mm and 120 mm respectively. The distance between the elastic agitator and the inlet, Le , the elastic agitator's material properties, angle of inclination and the elastic agitator geometry have direct effects in the FSI process. To evaluate the elastic agitator's stiffness effect on the thermal performance, all other parameters are kept constants. Le is 20 mm and $\alpha = 45^\circ$, while T_{wall} and T_{in} are 35°C



(a) Young's modulus 4e5 Pa



(b) Young's modulus 1e6Pa



(c) Young's modulus 4e6 Pa

Fig. 7. Maximum displacement in test case 1.

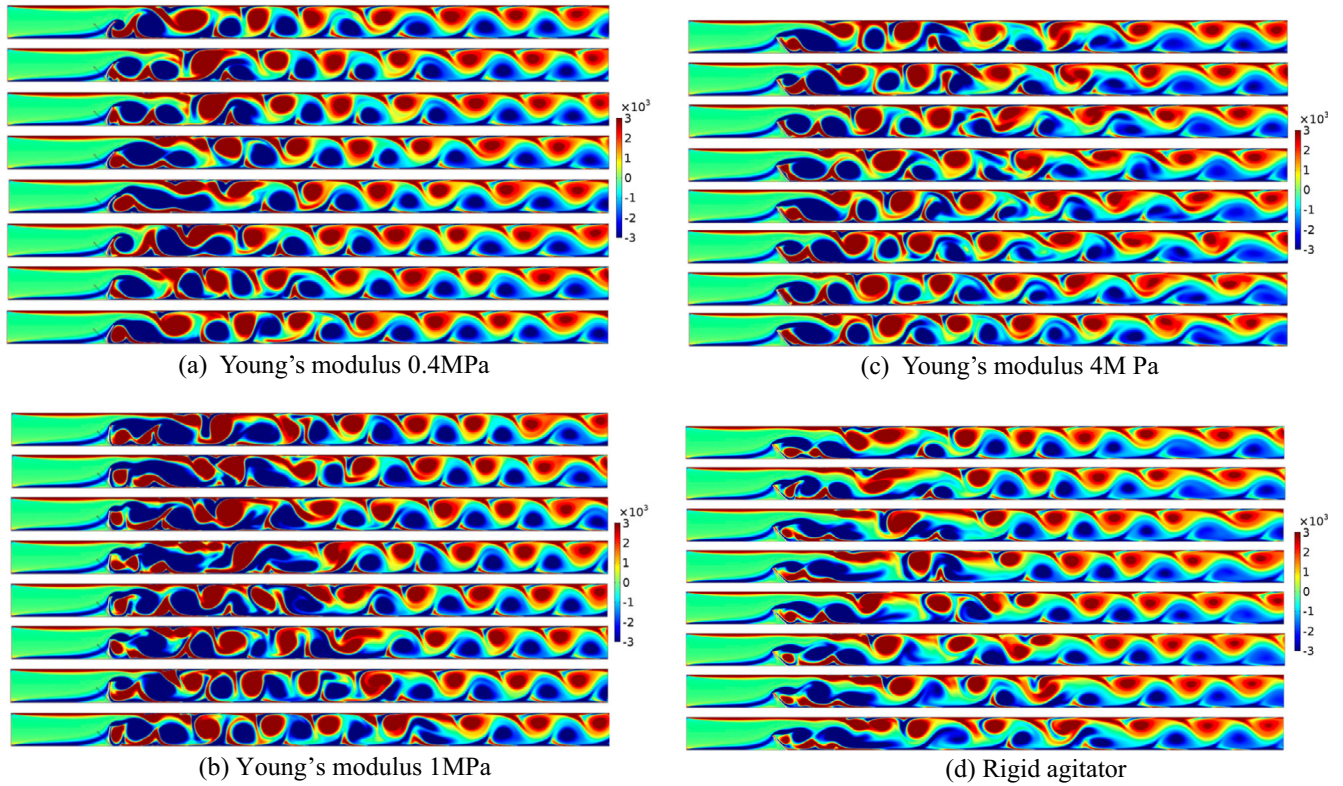


Fig. 8. Vorticity field in test case 1.

and 25 °C, respectively. The elastic agitator height and thickness are 5.7 mm and 0.2 mm. Three elastic agitators with different Young's Moduli (E) and one rigid agitator with the same geometry are compared for two inlet velocities: 3 m/s and 4 m/s (test case 1 and test case 2). Young's moduli in consideration are 0.4 MPa, 1.0 MPa and 4.0 MPa. A 0.2 mm thick agitator with E from 0.4 to 4.0 MPa is equivalent to a 0.025 mm thick one with E 0.2 to 2.0 GPa, which can be materials, such as polyethylene film and Kapton film. The equivalent relation is shown in S1.

The Reynolds number is the non-dimensional parameter used to determine laminar or turbulent flow which is given as

$$Re = \frac{u_{in} D_h \rho_0}{\mu} \quad (8)$$

where D_h is the hydraulic diameter equal to $2H$ in the 2-D case. Hence, Re in the two test cases is obtained as 2524 and 3365. In a 2-D very clean channel, turbulence begins for Re equal to 10,000 with the constant velocity inlet boundary condition [40–41]. In this article, we assume the two test cases are still laminar in the channel with the elastic agitators.

4.1. Grid independent study

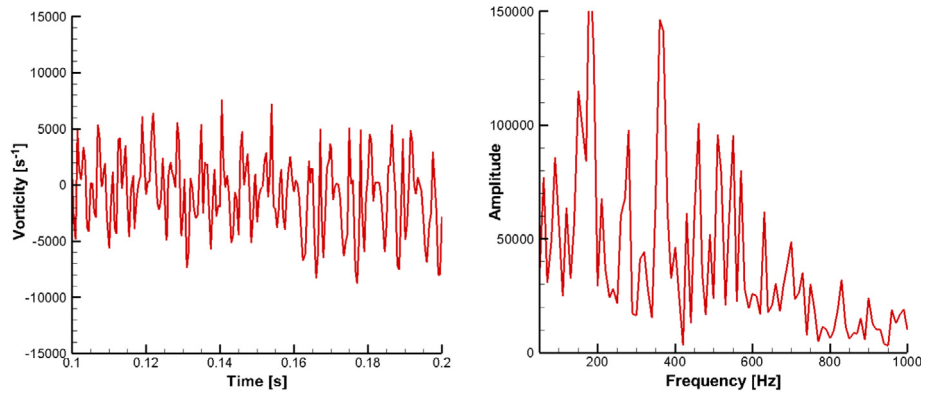
A grid independent study is performed before discussing the structure stiffness effects. Four different grids are employed to solve the same problem and they all use structured mesh for the boundary layer and unstructured mesh for the rest region. Different element size results in various grid numbers from 20,000 to 210,000. The inlet velocity, elastic agitator density and E are defined as 3 m/s, 125 kg/m³ and 0.40 MPa, respectively. Because the thermal performance of the elastic agitator is the main concern in this article, the average rejected heat, which is average heat flux, on the top and bottom is used to evaluate different grid results. Fig. 5(a) shows the results comparison for the different grids. Grid

3 and grid 4 reach good agreement in the amount of rejected heat. Grid 3 is chosen in this article to save computational resources while maintaining good accuracy. The grid settings near the elastic agitator are showing in Fig. 5(b).

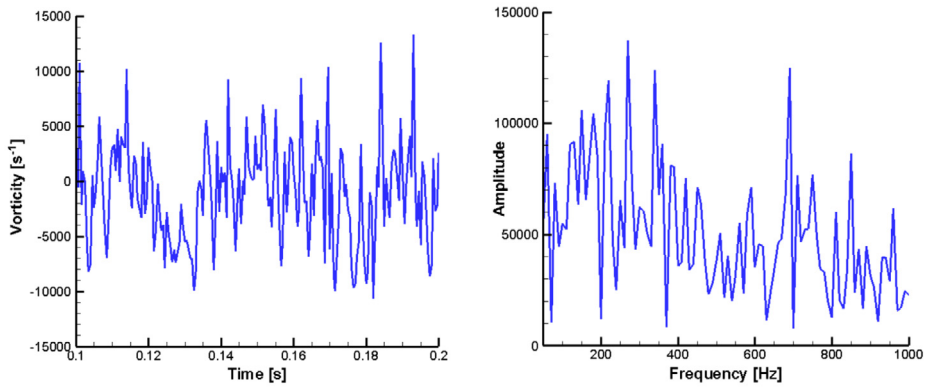
4.2. Test case 1 ($Re = 2524$)

For test case 1, the inlet velocity is 3 m/s and three different materials with $E = 0.40$ MPa, 1 MPa and 4 MPa are considered with the same density of 125 kg/m³. Fig. 6 shows the structure motions for the three materials from 0.19 s to 0.20 s. For the case with $E = 0.40$ MPa, the elastic agitator vibrates significantly while the maximum displacement is around 4.0 mm. In the case with $E = 1$ MPa, the elastic agitator vibrations are lower than the previous condition and the maximum displacement is around 2.8 mm. Increasing E to 4 MPa, the vibration in the elastic agitator is very limited and the maximum displacement is 0.4 mm. The maximum displacement is always at the tip of the elastic agitator.

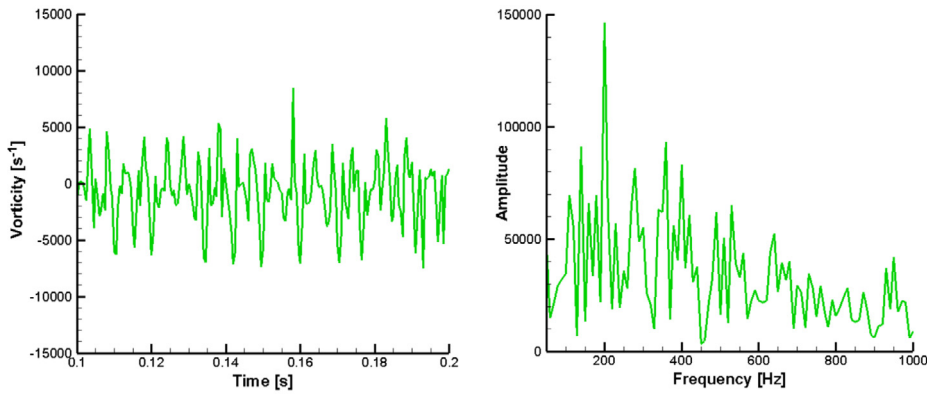
Fig. 7 shows the maximum displacements and corresponding Fourier analysis results for the different E . For $E = 0.40$ MPa, the maximum displacement oscillates around 4.0 mm and the fluctuation is within 0.5 mm. In the Fourier analysis results, two clear peaks appear at 200 Hz and 500 Hz. This indicates that the motion of the elastic agitator is a combination of two periodical results. Increasing E to 1 MPa, the maximum displacement oscillates around 2.8 mm and the fluctuation is within 0.2 mm. From the Fourier analysis, we can see several peaks between 100 Hz and 300 Hz with the dominant peak at 180 Hz. For the $E = 4$ MPa, the oscillations occur around the maximum displacement of 0.4 mm and the fluctuation is very limited. Fourier analysis shows two peaks at 180 Hz and 200 Hz, indicating the motion of elastic agitators is a combination of two periodical results. Therefore, the motions in these three conditions are quite different from one another.



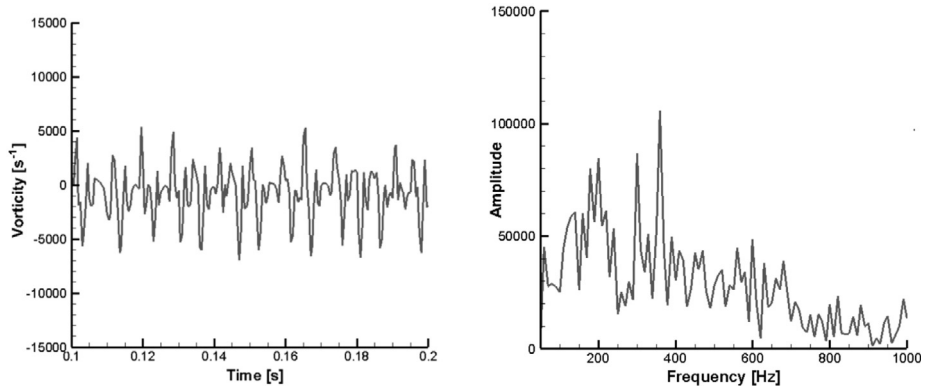
(a) Young's modulus 0.4MPa



(b) Young's modulus 1MPa

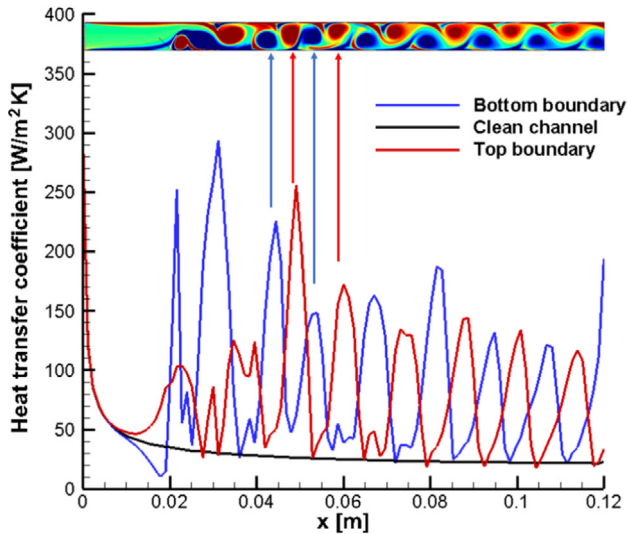


(c) Young's modulus 4MPa

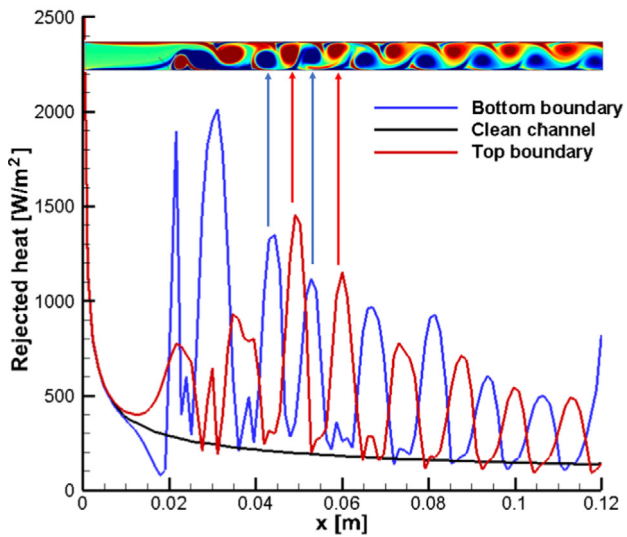


(d) Rigid agitator

Fig. 9. Vorticity tendency in test case 1.



(a) Heat transfer coefficient



(b) Rejected heat

Fig. 10. Local thermal performance in test case 1.

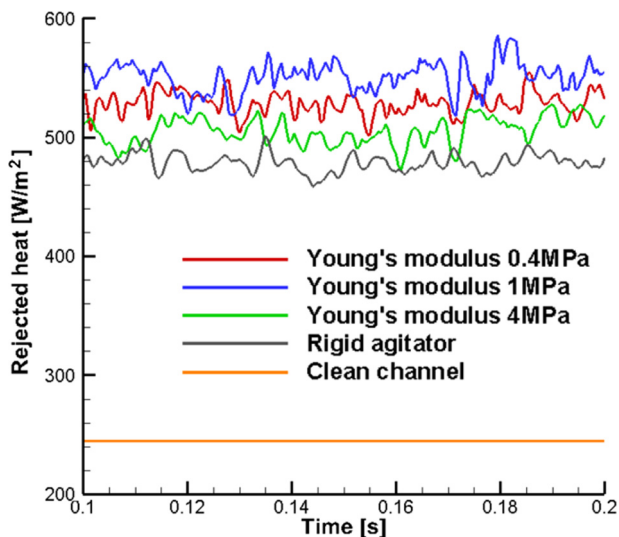


Fig. 11. Rejected heat comparison in test case 1.

Different motions cause various vortex generating processes. Vortices location and strength can be evaluated with the vorticity field. Fig. 8 shows the vorticity fields from 0.19 s to 0.20 s in different elastic agitator cases. The rigid agitator results are also included for comparison. In all of the conditions, a counterclockwise vortex continuously generates at the tip of agitator while a clockwise vortex generates between it and the bottom boundary. Then, this pair of vortices transfers to the downstream direction. With the same contour legend range, we can find vortices in the conditions with $E = 0.40$ MPa and 1 MPa are stronger than the other two cases.

To quantify the difference, vorticity tendencies at a chosen point B (40 mm, 1.65 mm) are compared for the three elastic agitators and rigid agitator as shown in Fig. 9. Vorticity fluctuation for $E = 1$ MPa is the highest and the rigid case is the lowest while the case with $E = 0.40$ MPa has stronger vorticity fluctuation than for the $E = 4$ MPa. In the Fourier analysis results, many frequency peaks appear in all four conditions, indicating results composed with several periodical modes.

The vortices generated during FSI have been discussed above. The main concern in this article is the thermal performance of the elastic agitators. Taking the $E = 0.40$ MPa as an example, the local thermal performance of the elastic agitator related to vorticity field at 0.02 s is shown in Fig. 10. The local heat transfer coefficient is defined as:

$$h = \frac{q}{T_{wall} - T_{average}} \quad (9)$$

where q is the local heat flux and $T_{average}$ is the average temperature for the local cross section. As shown in Fig. 10(a), the heat transfer coefficients are highest at the inlet due to entrance effects. As highlighted in the figure, many peaks exist on both the top and bottom of the channel. The heat transfer coefficient is enhanced locally at the vortex location. The heat transfer coefficient is enhanced locally up to 900% for $x = 0.03$ m, and all the peaks have more than 300% enhancement. Fig. 10(b) shows the local rejected heat of elastic agitator compared with the clean channel case. Similar to the heat transfer coefficient, the local rejected heat is also enhanced at the vortices locations. The rejected heat enhancement ratio is lower than that of the heat transfer coefficient because of $T_{average}$ increasing in the downstream direction.

Rejected heat comparisons among different agitators and the clean channel are shown in Fig. 11. All the agitators can enhance heat transfer significantly compared with the clean channel. All elastic agitators reject more heat than the rigid case. The FSI process can enhance the heat transfer when compared with the rigid agitator. Young's modulus of 1 MPa condition has the highest rejected heat while the $E = 0.40$ MPa condition is better than $E = 4$ MPa condition. These trends agree well with the vorticity results. Generating strong vortices is the key for the heat transfer enhancement.

4.3. Test case 2 ($Re = 3565$)

Test case 2 is simulated with an inlet velocity of 4 m/s, while the properties of elastic agitators are the same as those in test case 1. Fig. 12 shows the motions for three elastic agitators from 0.19 s to 0.20 s. Similar to test case 1, $E = 0.40$ MPa condition has the highest vibration amplitude, and $E = 4$ MPa condition has the lowest vibration amplitude. The vibration in test 2 is stronger than that in test case 1 for all three materials. The tip of elastic agitator has the maximum displacement. Fig. 13 shows the maximum displacement tendency for test case 2. In $E = 0.40$ MPa condition, the oscillations occur around the maximum displacement of 4.5 mm and the fluctuation is within 1.0 mm. Fourier analysis results show two peaks at 270 Hz and 520 Hz, indicating the motion is

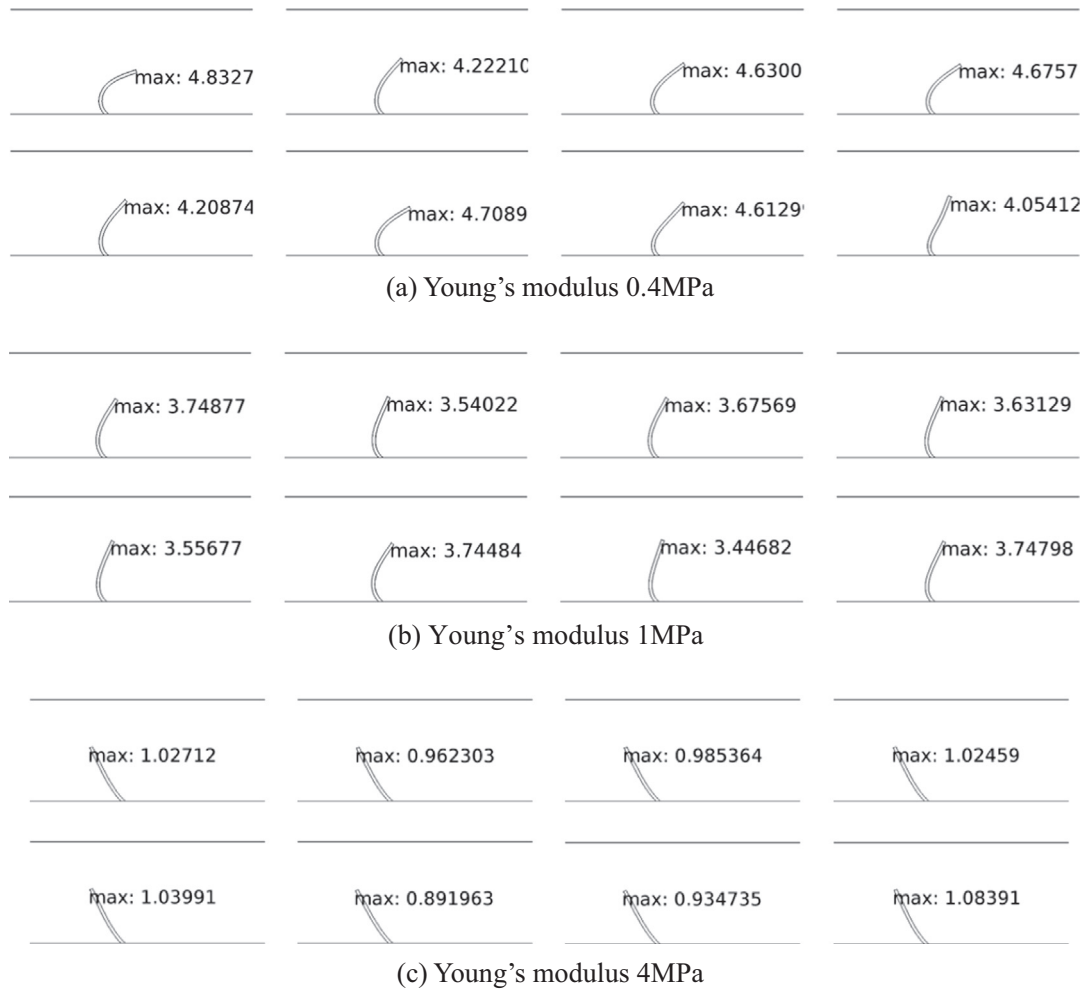


Fig. 12. Elastic agitator motion in test case 2.

composed with two periodical motions. In $E = 1$ MPa condition, the maximum displacement oscillates around 3.8 mm and the fluctuation is less than 0.5 mm. One clear peak is shown in the Fourier analysis results, showing the motion is periodical with 300 Hz frequency. In $E = 4$ MPa condition, the maximum displacement oscillates around 1.0 mm and the fluctuation is less than 0.1 mm. Two peaks can be found in the Fourier analysis results at 200 Hz and 320 Hz, showing the motion is a combination of two periodical motions.

The motions in test case 2 are different from those in test case 1 for all the elastic agitators. The maximum displacements and frequencies are stronger in test case 2. Different motions excite various vorticity fields and the rigid agitator is also used for evaluating the performance of elastic agitators. Fig. 14 shows the vorticity field for four agitators from 0.19 s to 0.20 s. One pair of vortices is generated after the agitator and transferred downstream. The generated vortex strength for elastic agitators is clearly stronger than that of the rigid agitator.

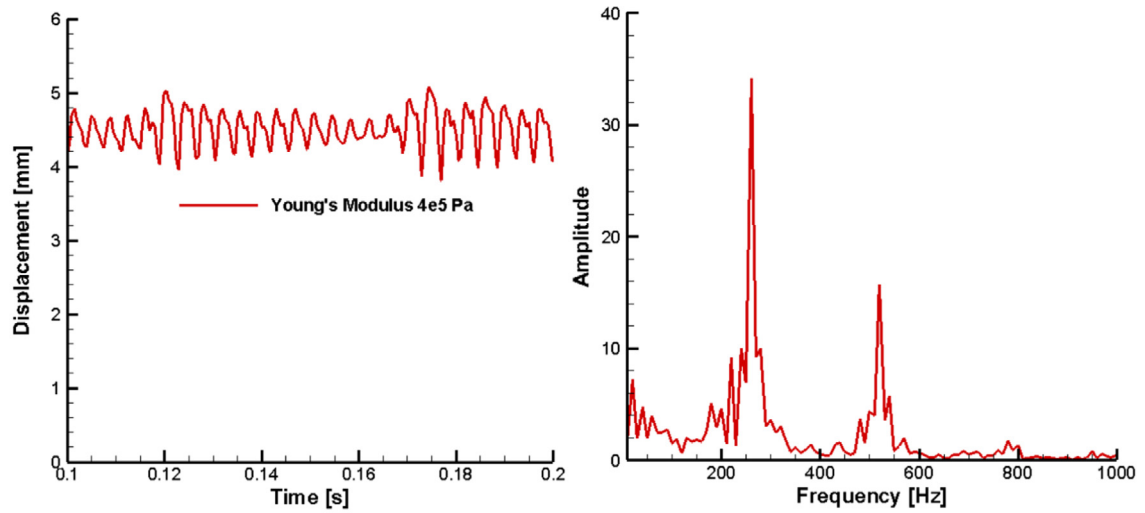
Fig. 15 shows the vorticity tendency at (40 mm, 1.65 mm) and corresponding Fourier analysis results. Many frequency peaks exist for all the four agitators, indicating the vorticity is composed of several periodical motions. The elastic agitator with $E = 1$ MPa shows the highest vorticity fluctuation and the rigid agitator shows the lowest. Different from test case 1, the case with $E = 4$ MPa has stronger vorticity fluctuation than $E = 0.40$ MPa condition in test case 2.

Taking $E = 0.40$ MPa case as an example, Fig. 16 includes the local thermal performance related to the vorticity field at 0.2 s. As found in test case 1, the heat transfer coefficient and rejected heat are enhanced at the vortex location. The rejected heat enhancement ratio over the clean channel is lower than that of the heat transfer coefficient because of T_{average} increasing in the downstream direction.

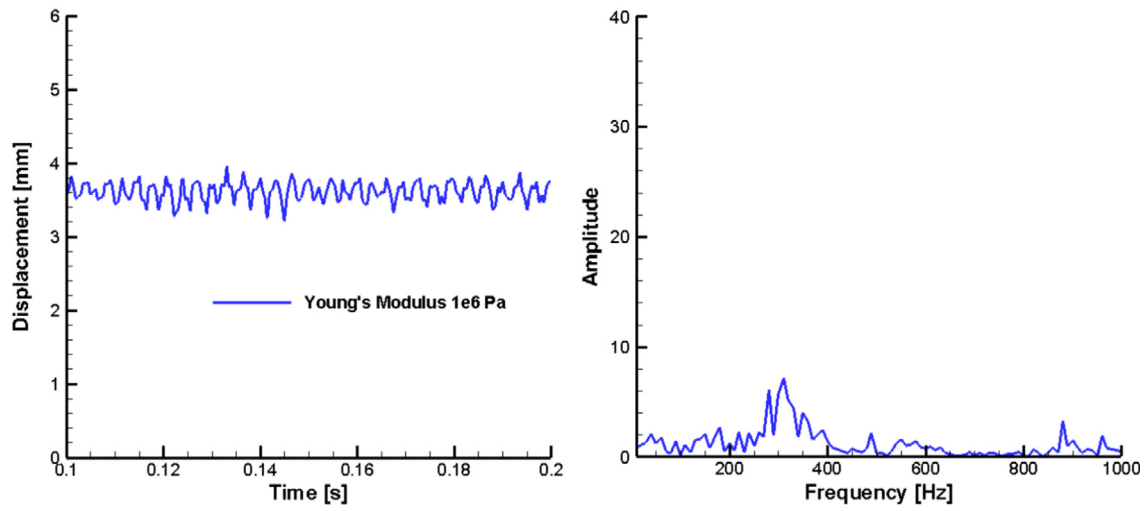
Fig. 17 shows the rejected heat comparison among different agitators and the clean channel. All of the agitators can enhance the rejected heat significantly compared with the clean channel, and the elastic agitators have higher performance than the rigid agitator. The $E = 1$ MPa condition has the highest rejected heat, and $E = 4$ MPa condition has higher performance than the $E = 0.40$ MPa. These trends agree well with vorticity field shown in Fig. 15.

4.4. Thermal performance comparison

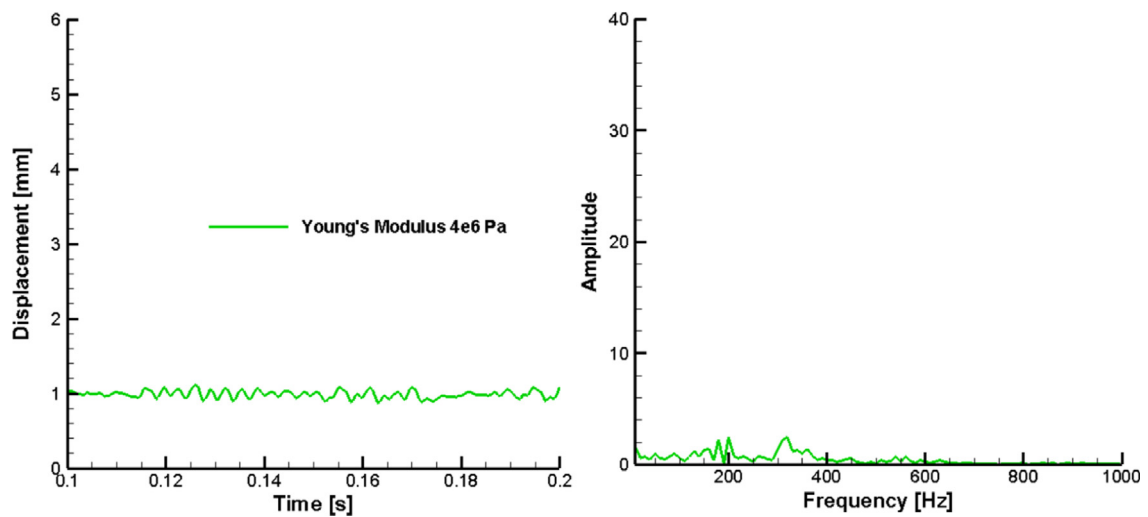
Fig. 18 shows the thermal performance of the various agitators and clean channel. At the same velocity, rejected heat can be enhanced by 140% using an elastic agitator with $E = 1$ MPa, as shown in Fig. 18(a). The results above focus on the heat rejection for different agitators. Pressure loss, which is total pressure difference between inlet and outlet of the channel, also increases because of the FSI process. To evaluate the thermal performance of the elastic agitator, pressure loss and rejected heat need to be considered. Pumping power is employed to make fair comparisons.



(a) Young's modulus 0.4MPa



(b) Young's modulus 1MPa



(c) Young's modulus 4MPa

Fig. 13. Maximum displacement in test case 2.

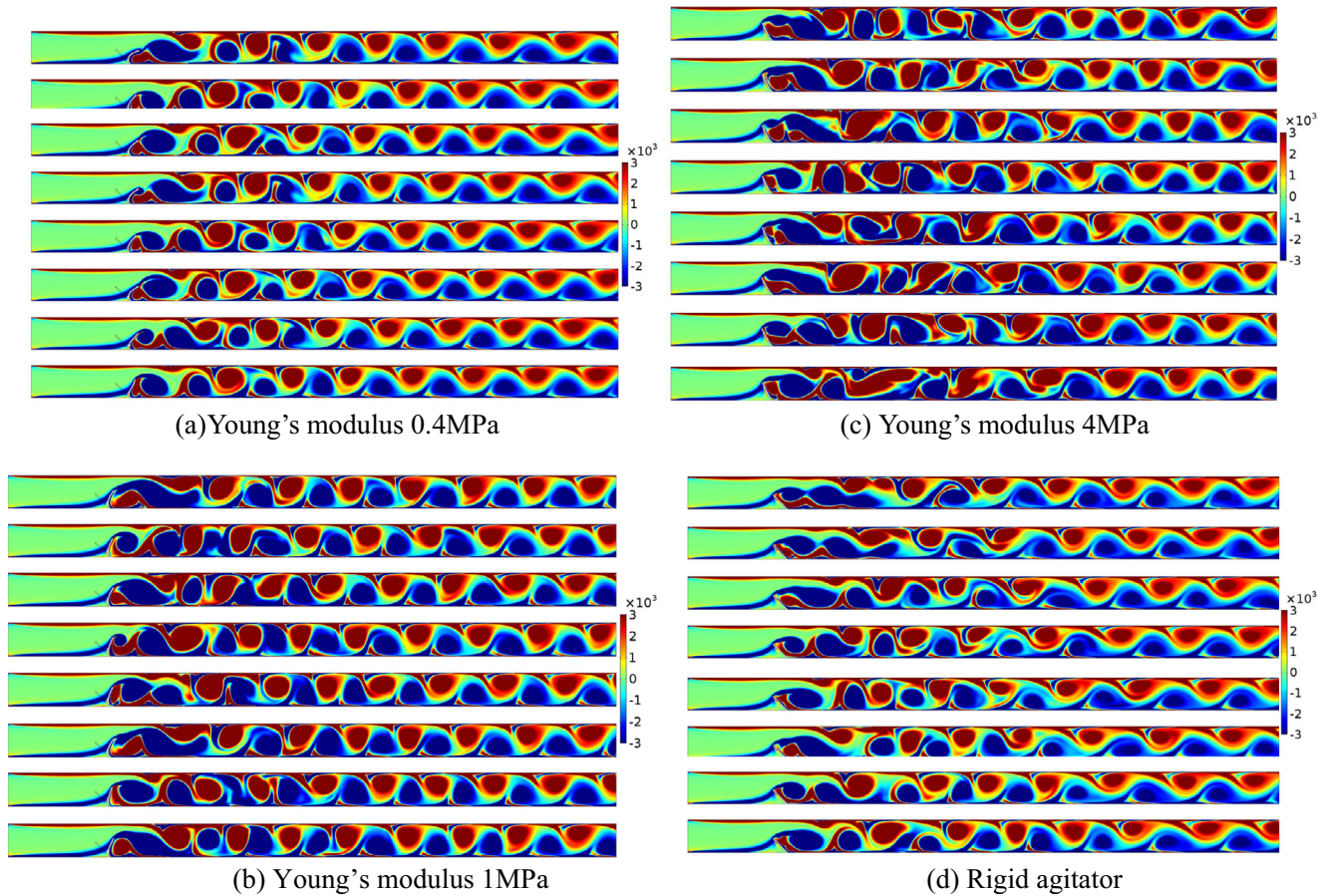


Fig. 14. Vorticity field in test case 2.

$$\text{Pumping power} = \text{pressure loss} \times \text{velocity} \quad (10)$$

Taking the total pressure loss between the inlet and outlet of the channel, the thermal performance comparison is shown in Fig. 18(b). Due to the pressure loss increase caused by agitators, the heat transfer enhancement ratio at same pumping power is lower than that at some velocity. The elastic agitator with $E = 0.40$ MPa has the highest enhancement ratio of 48% at the same pumping power. In a realistic engineering application, channel entrance and channel exit both cause pressure loss, we can use $0.5 \frac{\rho_0 V^2}{2}$ and $\frac{\rho_0 V^2}{2}$ to estimate these effects [44]. Fig. 18(c) shows the thermal performance comparison regarding the total pumping power. All agitators have similar heat transfer enhancement ratios, around 80%, and the $E = 1$ MPa condition has the highest one, 87%. Based on these results, the elastic agitator with $E = 1$ MPa is preferred.

The average Nusselt number is the non-dimensional parameter used to evaluate the convective heat transfer capability, which is defined as

$$Nu_{ave} = \frac{h_{ave} D_h}{k}, \quad (11)$$

where average heat transfer coefficient, h_{ave} , is calculated as the rejected heat divided by the logarithmic mean temperature difference. Fig. 19 shows the results of channels with different agitators compared with the clean channel. With same Re , channels with agitators have much higher Nu compared with a clean one while elastic agitators have better performance than the rigid one. The elastic agitator with $E = 1$ MPa has the best performance and can improved

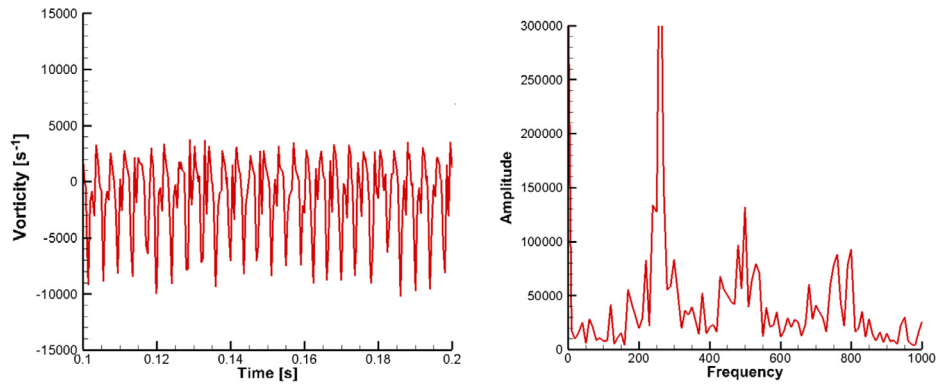
the average Nusselt number in the channel by 200% compared with the clean one.

4.5. Dynamics modal decomposition for FSI

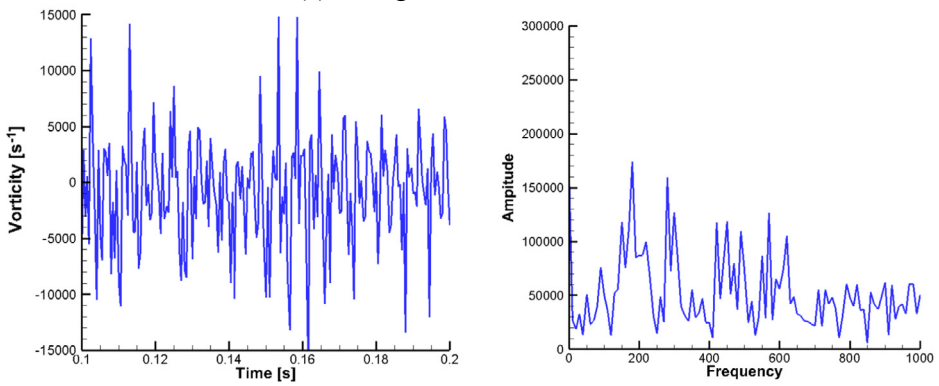
Different vortex generators can achieve various vorticity fields. Local heat transfer coefficients and rejected heat rates are enhanced at the vortex location based on Figs. 10 and 16. Thermal performance is maximized when large modulations are created at the boundary layer of the channel, while at the same time avoiding the creation of strong vortices in the other regions of the channel [45]. However, the quantitative relation between vortices and temperature field remains deficient, which is fundamental to the internal convective heat transfer performance.

To address this, this work uses the vorticity fluctuation at the chosen point B to evaluate the thermal performance for the first time. As shown in Figs. 8 and 14, the distances between the centers of transient vortices and channel boundaries are close to each other for different vortex generators. Vorticity fluctuation at the chosen point B can indicate the vortices impacts to the thermal boundary layer. Therefore, heat transfer is further improved with a higher vorticity fluctuation.

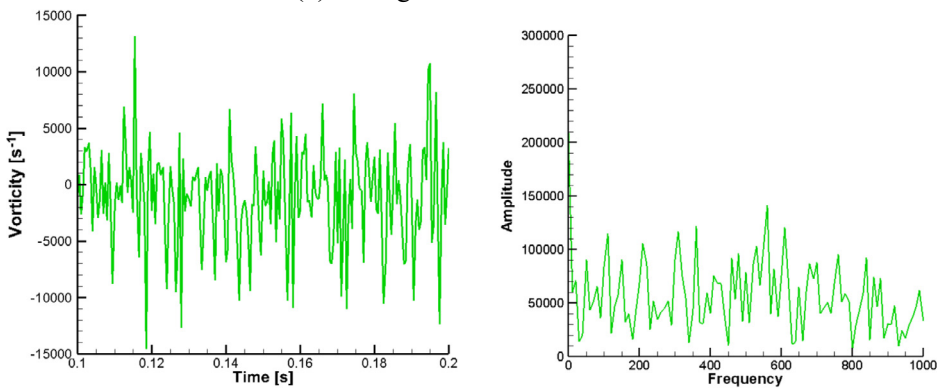
Transient results are obtained for different vortex generators and the time average data is used to evaluate the thermal performance. To explore the quantitative relation between vortices and thermal performance, modal analysis is carried out. Dynamic modal decomposition [46–48] is performed in this work with the transient results for different vortex generators at 4 m/s. As discussed in Section 4.4, the $E = 1$ MPa condition has the highest rejected heat, and the $E = 4$ MPa condition has higher performance



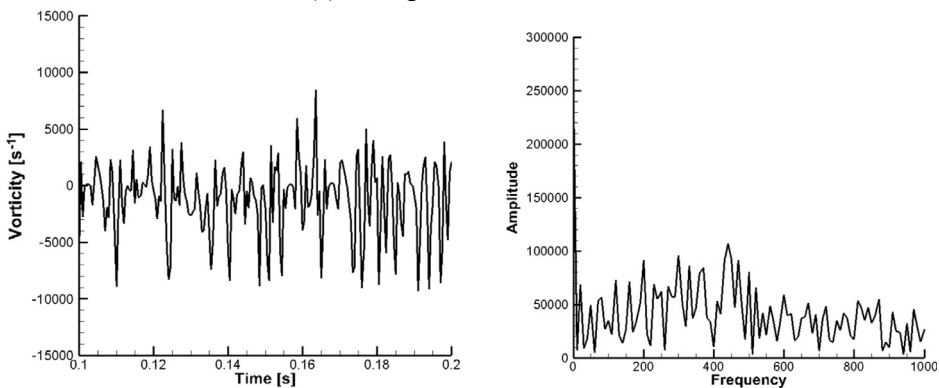
(a) Young's modulus 0.4MPa



(b) Young's modulus 1MPa

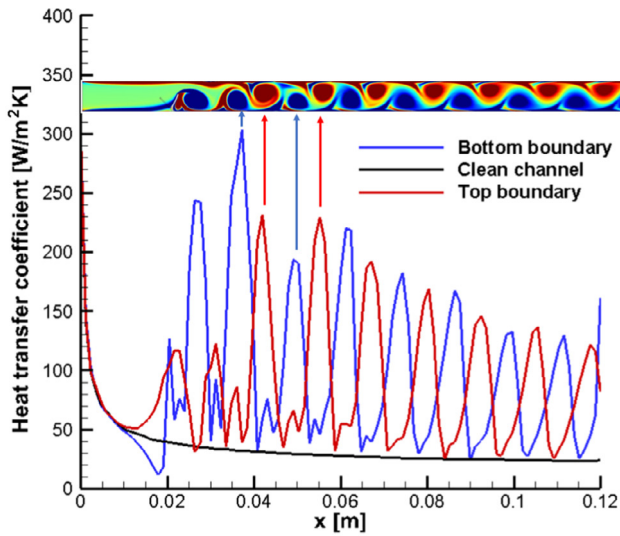


(c) Young's modulus 4MPa

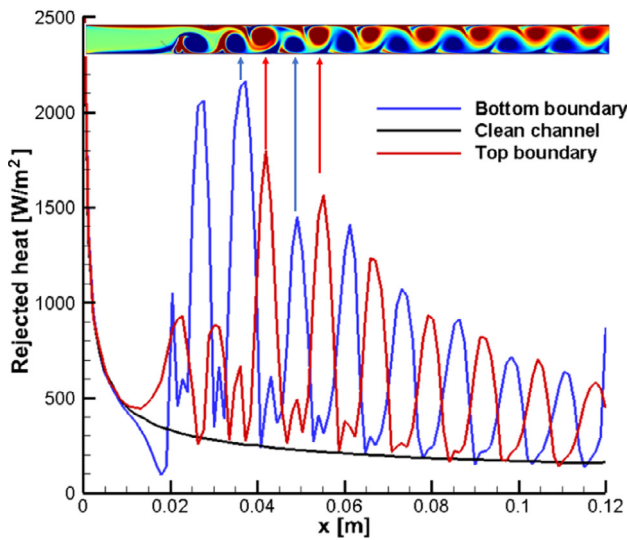


(d) Rigid agitator

Fig. 15. Vorticity tendency in test case 2.



(a) Local heat transfer coefficient



(b) Local rejected heat

Fig. 16. Local thermal performance in test case 2.

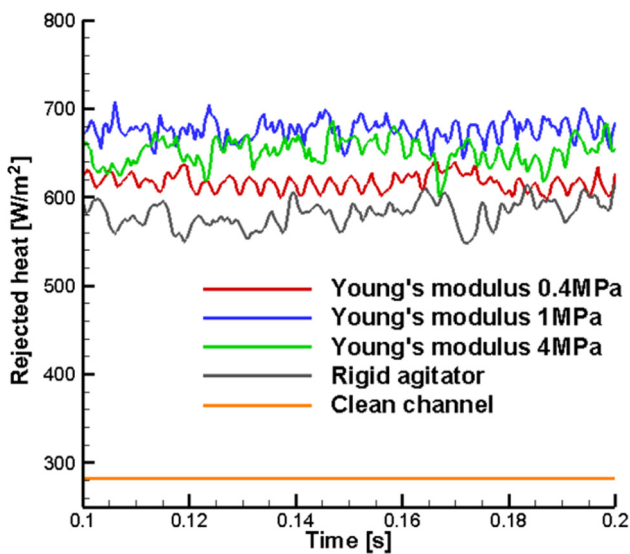
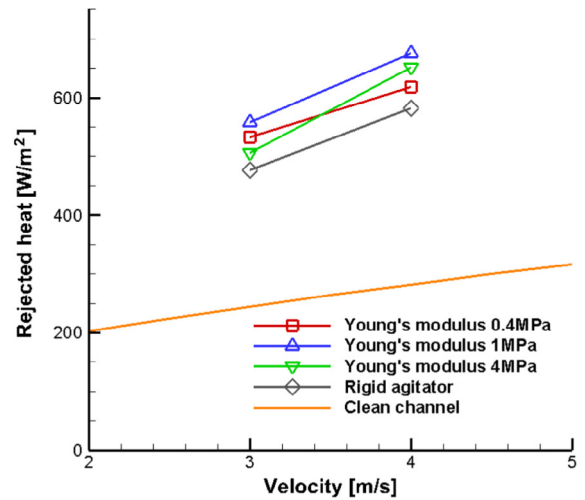
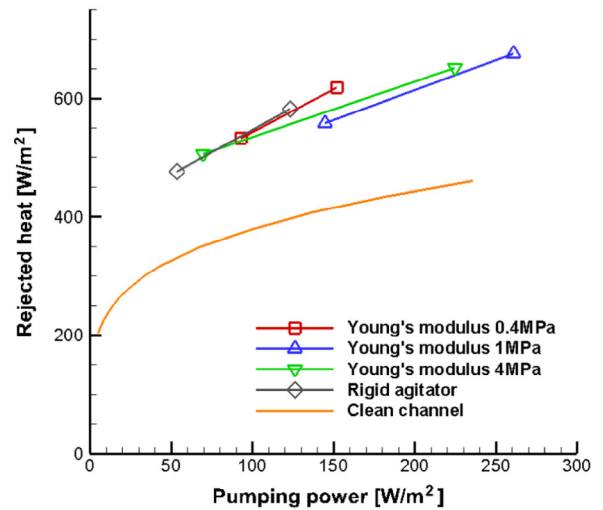


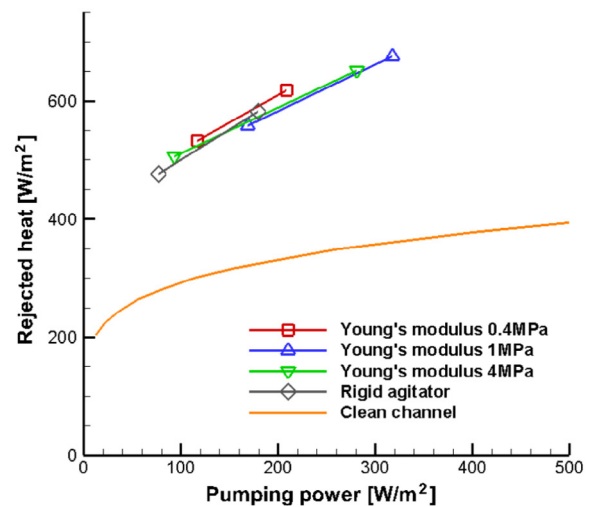
Fig. 17. Reject heat comparison in test case 2.



(a) Results comparison based on velocity



(b) Results comparison based on channel pumping power



(c) Results comparison based on total pumping power

Fig. 18. Thermal performance comparison.

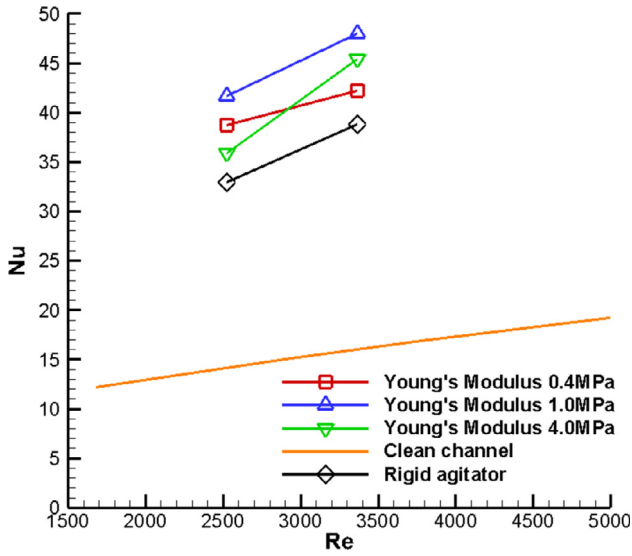


Fig. 19. Average Nu comparison for different vortex generators.

than the $E = 0.40$ MPa case, while all of the elastic agitators show advantages over a rigid one. The selected computational region is behind agitator from 40 mm to 120 mm.

In the modal analysis, steady and oscillating modes are achieved for different agitators. Fig. 20 shows the steady modes of temperature field for different vortex generators which will not change with time and they are quite different from each other. We can see the better performance condition have higher temperature in the channel. It is because working fluid temperature increases faster in better performance condition.

Fig. 21 shows the local rejected heat comparison between instantaneous simulation result and corresponding steady mode for different vortex generators. Several peaks exist in the instantaneous simulation results where the vortices locate. These peaks will change locations as the vortices transfer to downstream

direction. On the other hand, the local rejected heat will not change with time in the steady mode. Table 2 shows the average rejected heat comparison between simulation and corresponding steady mode for different vortex generators. We can find that the results from steady mode are very close to the average rejected heat calculated from simulation directly. In the meantime, better performance case has higher rejected heat in steady mode. It is necessary to point out the results from steady mode are all lower those from instantaneous simulation results. It is because the selected computational region is behind agitator from 40 mm to 120 m in modal analysis and the inlet high performance effect does not contribute to the steady mode results. Therefore, thermal performance is strongly related with the steady mode of temperature field.

Fig. 22 shows the steady mode of vorticity and it relates to the steady mode of temperature directly. We can see very continuous contour near the boundaries in the rigid agitator condition while the contour near boundaries for the $E = 1$ MPa condition has most discrete patterns compared with the other conditions. More discrete vorticity patterns in steady mode near the boundaries have stronger impact at breaking the boundary layer, which can lead to better performance. Therefore, creating more discrete patterns near the boundaries of the steady mode in the vorticity field can enhance the internal convective heat transfer.

5. Conclusion

In this article, flapping vortex generators are investigated numerically for heat transfer enhancement. Elastic agitators are mounted on the fin to form the flapping vortex generator and different E are compared to study the effects of agitator stiffness. Three E considered result in various elastic agitator motions due to the fluid-structure interactions. Correspondingly, the vortices generated and transfer processes are also different for the three conditions, which leads to the different thermal performance. Three elastic agitators and one rigid agitator are analyzed under two velocities, while the results are compared with those of the clean channel. Numerical results show that the elastic agitator can enhance the channel heat transfer significantly, and

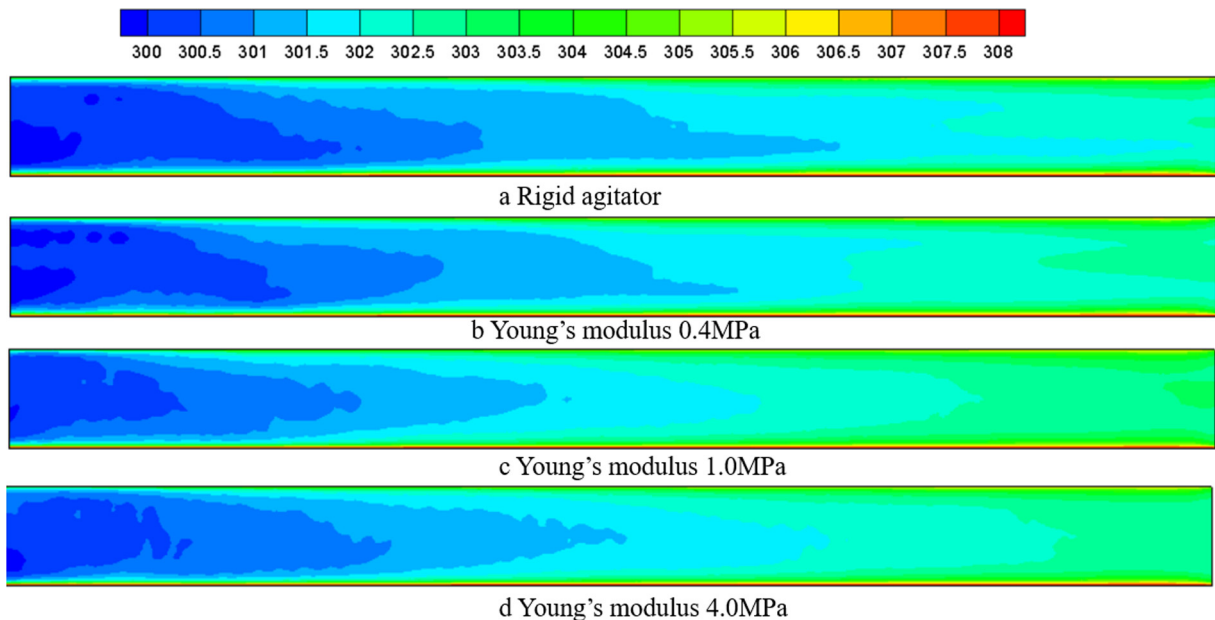


Fig. 20. Steady modes of temperature field for different vortex generators.

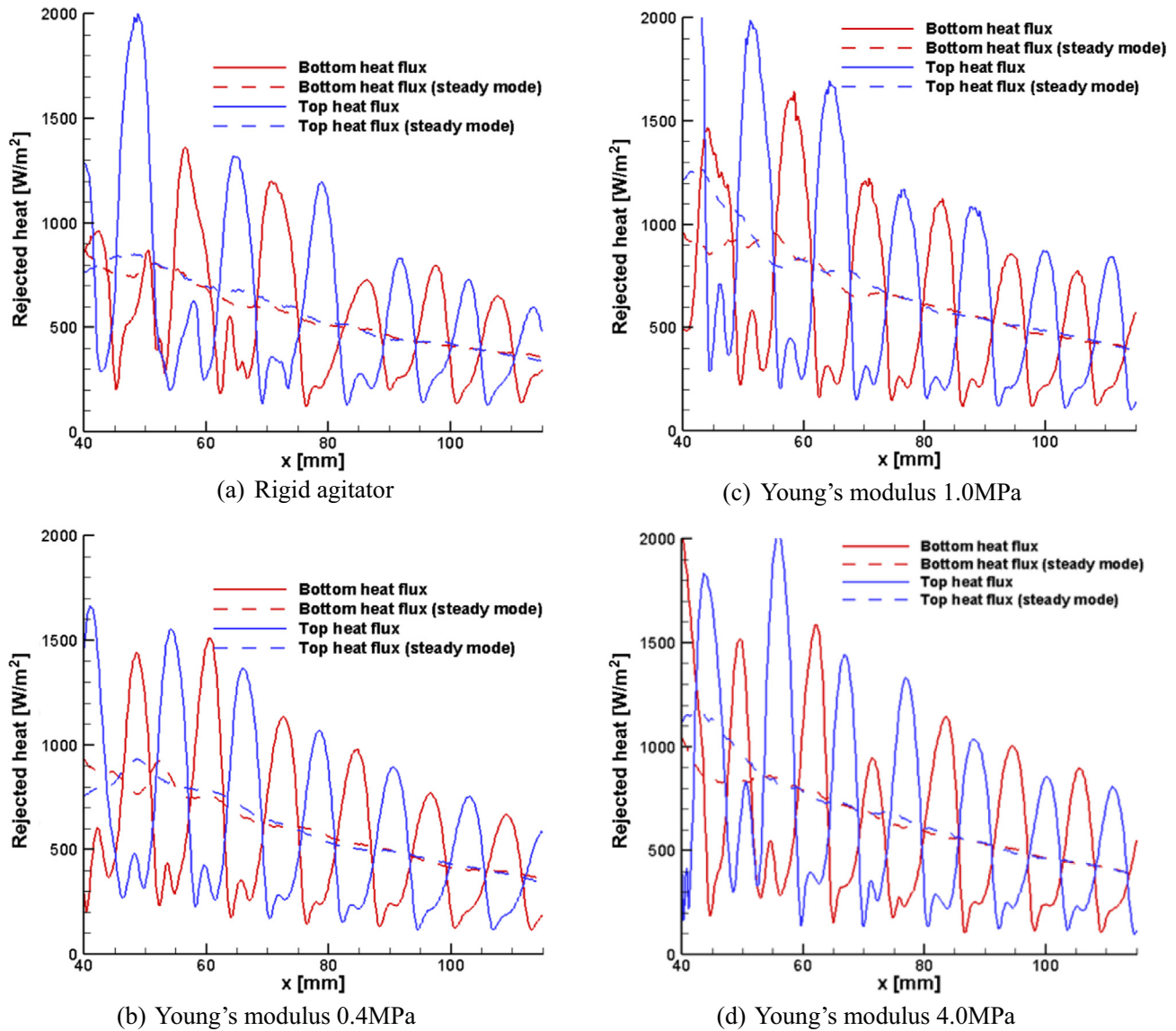


Fig. 21. Local rejected heat comparison between instantaneous simulation result and corresponding steady mode for different vortex generators.

Table 2

Average rejected heat comparison between simulation and corresponding steady mode for different vortex generators.

	Average rejected heat from steady mode (W/m ²)	Average rejected heat from simulation (W/m ²)
Rigid agitator	558	581
Young's modulus 0.4 MPa	588	618
Young's modulus 1.0 MPa	660	676
Young's modulus 4.0 MPa	641	651

$E = 1$ MPa condition has the best performance, capable of enhancing the rejected heat by 140% at the same velocity and 87% at the same total pumping power. The average Nusselt number can be improved up to 200% with the same Reynolds number.

The distances between centers of transient vortices and channel boundaries are close to each other for different vortex generators. Vorticity fluctuation at the chosen point B can indicate the vorticities

impacts to the thermal boundary layer. Therefore, heat transfer is further improved with a higher vorticity fluctuation. Modal analysis is performed with transient temperature and vorticity results using dynamic modal decomposition. It can be shown that steady modal behavior directly relates to the thermal performance of the system. Furthermore, creating more discrete patterns near the boundaries of the steady mode in the vorticity field can enhance the internal convective heat transfer.

Acknowledgement

The authors greatly appreciate the support of ARPA-E under Grant No. DE-AR0000582. The authors would like to acknowledge Brian J. Hernan and Miles V. Barnhart for their constructive comments.

Conflicts of interest statement

The authors declared that there is no conflict of interest.

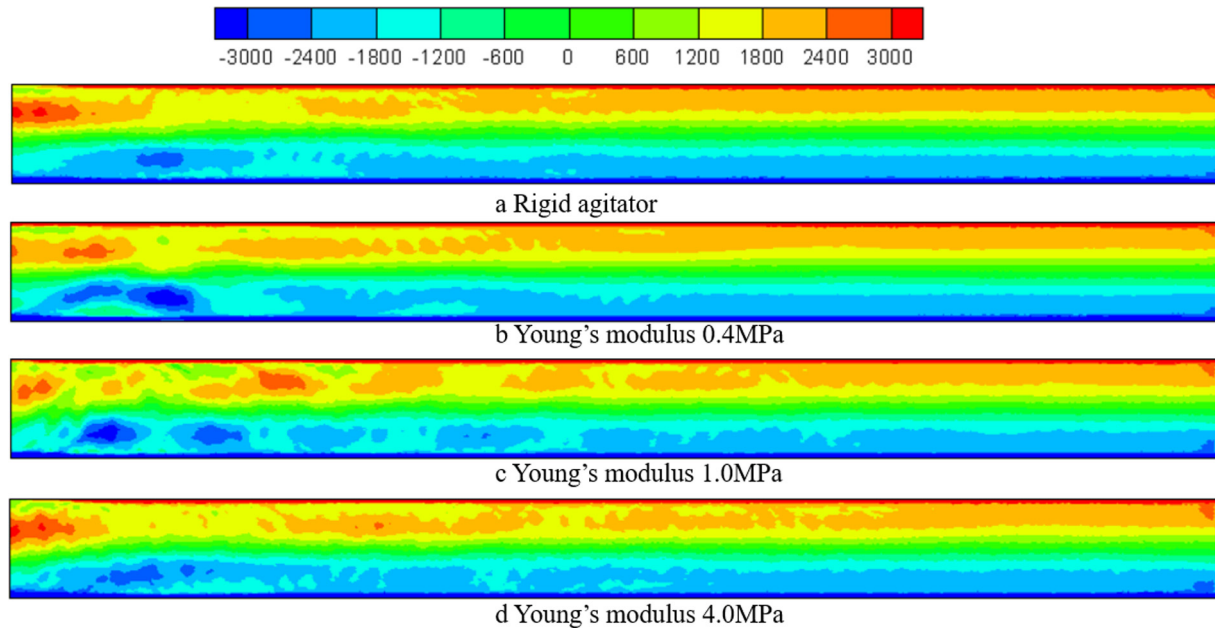


Fig. 22. Steady modes of vorticity field for different vortex generators.

Appendix A. Supplementary material

Supplementary data associated with this article can be found, in the online version, at <https://doi.org/10.1016/j.ijheatmasstransfer.2017.11.067>.

References

- [1] H. Kim et al., Water harvesting from air with metal-organic frameworks powered by natural sunlight, *Science* 8743 (April) (2017) 1–10.
- [2] S.C. Davis, W. Hay, J. Pierce, *Water in the Energy Industry: An Introduction*, BP, 2014.
- [3] Z. Li, M. Yang, Y. Zhang, A coupled lattice Boltzmann and finite volume method for natural convection simulation, *Int. J. Heat Mass Transf.* 70 (2014) 864–874.
- [4] Z. Li, M. Yang, Y. Zhang, Hybrid Lattice Boltzmann and Finite Volume Method for Natural Convection, *J. Thermophys. Heat Transf.* 28 (1) (2014) 68–77.
- [5] Z. Li, M. Yang, Y. Zhang, Lattice Boltzmann method simulation of 3-D natural convection with double MRT model, *Int. J. Heat Mass Transf.* 94 (2016) 222–238.
- [6] H. Xu et al., Coupled natural convection and radiation heat transfer of hybrid solar energy conversion system, *Int. J. Heat Mass Transf.* 107 (2017) 468–483.
- [7] S. Caliskan, Experimental investigation of heat transfer in a channel with new winglet-type vortex generators, *Int. J. Heat Mass Transf.* 78 (2014) 604–614.
- [8] M. Fiebig, Vortices, generators and heat transfer, *Chem. Eng. Res. Des.* 76 (2) (1998) 108–123.
- [9] M.J. Lawson, K.A. Thole, Heat transfer augmentation along the tube wall of a louvered fin heat exchanger using practical delta winglets, *Int. J. Heat Mass Transf.* 51 (9–10) (2008) 2346–2360.
- [10] S. Liu, M. Sakr, A comprehensive review on passive heat transfer enhancements in pipe exchangers, *Renew. Sustain. Energy Rev.* 19 (2013) 64–81.
- [11] C. Min et al., Experimental study of rectangular channel with modified rectangular longitudinal vortex generators, *Int. J. Heat Mass Transf.* 53 (15–16) (2010) 3023–3029.
- [12] M. Oneissi et al., Novel design of delta winglet pair vortex generator for heat transfer enhancement, *Int. J. Therm. Sci.* 109 (2016) 1–9.
- [13] P.A. Sanders, K.A. Thole, Effects of winglets to augment tube wall heat transfer in louvered fin heat exchangers, *Int. J. Heat Mass Transf.* 49 (21–22) (2006) 4058–4069.
- [14] M. Sheikholeslami, M. Gorji-Bandpy, D.D. Ganji, Review of heat transfer enhancement methods: Focus on passive methods using swirl flow devices, *Renew. Sustain. Energy Rev.* 49 (2015) 444–469.
- [15] K. Torii, K.M. Kwak, K. Nishino, Heat transfer enhancement accompanying pressure-loss reduction with winglet-type vortex generators for fin-tube heat exchangers, *Int. J. Heat Mass Transf.* 45 (18) (2002) 3795–3801.
- [16] J.M. Wu, W.Q. Tao, Numerical study on laminar convection heat transfer in a channel with longitudinal vortex generator. Part B: Parametric study of major influence factors, *Int. J. Heat Mass Transf.* 51 (13–14) (2008) 3683–3692.
- [17] J.M. Wu, W.Q. Tao, Numerical study on laminar convection heat transfer in a rectangular channel with longitudinal vortex generator. Part A: Verification of field synergy principle, *Int. J. Heat Mass Transf.* 51 (5–6) (2008) 1179–1191.
- [18] K. Yang et al., On the heat transfer characteristics of heat sinks : with and without vortex generators, *IEEE Trans. Compon. Pack. Technol.* 33 (2) (2010) 391–397.
- [19] A. Beskok et al., Heat transfer enhancement in a straight channel via a rotationally oscillating adiabatic cylinder, *Int. J. Therm. Sci.* 58 (2012) 61–69.
- [20] B. Celik, M. Raisee, A. Beskok, Heat transfer enhancement in a slot channel via a transversely oscillating adiabatic circular cylinder, *Int. J. Heat Mass Transf.* 53 (4) (2010) 626–634.
- [21] W.S. Fu, B.H. Tong, Numerical investigation of heat transfer characteristics of the heated blocks in the channel with a transversely oscillating cylinder, *Int. J. Heat Mass Transf.* 47 (2) (2004) 341–351.
- [22] M. Pourgholam et al., Convective heat transfer enhancement in a parallel plate channel by means of rotating or oscillating blade in the angular direction, *Appl. Therm. Eng.* 78 (2015) 248–257.
- [23] J. Bae et al., Flutter-driven triboelectrification for harvesting wind energy, *Nat. Commun.* 5 (2014) 4929.
- [24] A.D. Becker et al., Hydrodynamic schooling of flapping swimmers, *Nat. Commun.* 6 (May) (2015) 8514.
- [25] M.L. Facchinetti, E. de Langre, F. Billoy, Coupling of structure and wake oscillators in vortex-induced vibrations, *J. Fluids Struct.* 19 (2) (2004) 123–140.
- [26] J.P. Gomes, H. Lienhart, Fluid–structure interaction-induced oscillation of flexible structures in laminar and turbulent flows, *J. Fluid Mech.* 715 (2013) 537–572.
- [27] M.J. Shelley, J. Zhang, Flapping and Bending Bodies Interacting with Fluid Flows, *Annu. Rev. Fluid Mech.* 43 (2011) 449–465.
- [28] N. Srinil, Multi-mode interactions in vortex-induced vibrations of flexible curved/straight structures with geometric nonlinearities, *J. Fluids Struct.* 26 (7–8) (2010) 1098–1122.
- [29] N. Srinil, H. Zanganeh, Modelling of coupled cross-flow/in-line vortex-induced vibrations using double Duffing and van der Pol oscillators, *Ocean Eng.* 53 (2012) 83–97.
- [30] F. Herrault et al., Cooling performance of micromachined self-oscillating reed actuators in heat transfer channels with integrated diagnostics, in: *Proceedings of the IEEE International Conference on Micro Electro Mechanical Systems (MEMS)*, (February), 2012, pp. 1217–1220.
- [31] P. Hidalgo, A. Glezer, Direct actuation of small-scale motions for enhanced heat transfer in heated channels. *Annual IEEE Semiconductor Thermal Measurement and Management Symposium*, 2014, pp.17–23.
- [32] P. Hidalgo, S. Jha, A. Glezer, Enhanced Heat Transfer in Air Cooled Heat Sinks Using Aeroelastically Fluttering Reeds Reed Motion and Flow Characterization, *21st International Workshop on Thermal Investigations of ICs and Systems (THERMINIC)*, 2015 (October).
- [33] K. Kota et al., Hybrid liquid immersion and synthetic jet heat sink for cooling 3-D stacked electronics, *IEEE Trans. Compon. Pack. Manuf. Technol.* 2 (5) (2012) 817–824.
- [34] J. Shi et al., Numerical study of heat transfer enhancement of channel via vortex-induced vibration, *Appl. Therm. Eng.* 70 (1) (2014) 838–845.

- [35] J.S. Go, Design of a microfin array heat sink using flow-induced vibration to enhance the heat transfer in the laminar flow regime, *Sens. Actuators, A* 105 (2) (2003) 201–210.
- [36] S. Ali et al., Heat transfer and mixing enhancement by using multiple freely oscillating flexible vortex generators, *Appl. Therm. Eng.* 105 (2016) 276–289.
- [37] S. Ali et al., Three-dimensional numerical study of heat transfer and mixing enhancement in a circular pipe using self-sustained oscillating flexible vorticity generators, *Chem. Eng. Sci. J.* 162 (2017) 152–174.
- [38] E.D. Tytell et al., Role of body stiffness in undulatory swimming: Insights from robotic and computational models, *Phys. Rev. Fluids* 1 (7) (2016) 73202.
- [39] K. Taira et al., Modal Analysis of Fluid Flows: An Overview, 2017, pp. 1–46. Available at: <<http://arxiv.org/abs/1702.01453>>.
- [40] J.P. Abraham, E.M. Sparrow, W.J. Minkowycz, Internal-flow Nusselt numbers for the low-Reynolds-number end of the laminar-to-turbulent transition regime, *Int. J. Heat Mass Transf.* 54 (1–3) (2011) 584–588.
- [41] W.J. Minkowycz, J.P. Abraham, E.M. Sparrow, Numerical simulation of laminar breakdown and subsequent intermittent and turbulent flow in parallel-plate channels: Effects of inlet velocity profile and turbulence intensity, *Int. J. Heat Mass Transf.* 52 (17–18) (2009) 4040–4046.
- [42] F.-B. Tian et al., Fluid–structure interaction involving large deformations: 3D simulations and applications to biological systems Available at: *J. Comput. Phys.* 258 (2014) 451–469. <http://linkinghub.elsevier.com/retrieve/pii/S0021999113007237>.
- [43] S. Turek, J. Hron, Proposal for numerical benchmarking of fluid-structure interaction between an elastic object and laminar incompressible flow, *Lect. Notes Comput. Sci. Eng.* 53 (2006) 371.
- [44] E. Shashi Menon, P.E.: *Piping Calculations Manual (Chapter 3)*, McGraw Hill Professional, Access Engineering, 2005.
- [45] K. Shoele, R. Mittal, Computational study of flow-induced vibration of a reed in a channel and effect on convective heat transfer, *Phys. Fluids* 26 (12) (2014).
- [46] C.W. Rowley et al., Spectral analysis of nonlinear flows Available at: *J. Fluid Mech.* 641 (2009) 115. http://www.journals.cambridge.org/abstract_S0022112009992059.
- [47] C.W. Rowley, S.T.M. Dawson, Model Reduction for Flow Analysis and Control Available at: *Annu. Rev. Fluid Mech.* 49 (1) (2017) 387–417. <http://www.annualreviews.org/doi/10.1146/annurev-fluid-010816-060042>.
- [48] P.J. Schmid, Dynamic mode decomposition of numerical and experimental data Available at: *J. Fluid Mech.* 656 (2010) 5–28. http://www.journals.cambridge.org/abstract_S0022112010001217.